LAST COPY

Quasi-static and Dynamic Crack Growth Along Bimaterial Interfaces: A Note on Crack-tip Field Measurements Using Coherent Gradient Sensing

by H.V. Tippur and A.J. Rosakis

ABSTRACT—The paper presents a preliminary experimental investigation of crack-tip deformation fields near quasi-statically and dynamically growing cracks in bimaterial interfaces. A three-point-bend bimaterial specimen with a relatively large stiffness mismatch between the two materials is studied. A recently developed optical method of coherent gradient sensing (CGS) is used to map crack-tip deformation fields.

The quasi-static measurements are interpreted using plane-stress, singular-field solution for the interface crack tip. Results are compared with two-dimensional finite-element computations performed on identical specimen geometries and material mismatch.[32] Impact studies conducted with bimaterial specimens provide the first experimental results of deformation fields near dynamically growing cracks along interfaces. Very high crack velocities, up to 80 percent of the Rayleigh wave speed for the less stiffer material of the two, are observed.

Introduction

Modeling crack-tip fields, crack initiation and crack growth in bimaterial interfaces is essential for understanding failure processes in advanced materials such as composites and ceramics. As early as 1959, Williams[1] examined local stress fields near a crack tip in a bimaterial interface and observed an oscillatory stress singularity of the form $r^{-1/2+i\epsilon}$ for traction-free boundary conditions on the crack surfaces. Since then, Sih and Rice,[2] Rice and Sih[3] have provided explicit expressions for the near-tip stresses and related them to remote elastic stress fields. Works of Erdogan,[4] England[5] and Malyshev and Salganik[6] have also further examined two-dimensional singular models for single or multiple crack geometries. The most physically unrealistic feature of these solutions is that they predict interpenetration of the crack flanks. This in turn contradicts the assumption of traction-free crack surfaces in the models. In an attempt to rid the model of this contradiction, Comninou[7] suggested a model with frictionless contact of the crack surfaces. Although this eliminated the problem of interpenetration of the crack faces, it led to a surprising result, namely the interface crack tip has a zero K_1 and nonzero K_2 under purely tensile remote loading. The contact-zone size predicted in such models is a strong function of the nature of remote in-plane loading.[7,8] Knowles and Sternberg,[9] on the other hand, have considered a crack between two dissimilar, incompressible, neo-Hookean sheets and have shown that within the framework of nonlinear, plane stress, elastostatics, the oscillatory part of the singularity disappears. A very detailed two-dimensional finite-element computation performed recently by Shih and Asaro[10] under small-scale yielding conditions has shown that the oscillatory singularity is a strong function of material-hardening characteristics and oscillations disappear at rather low remote stress levels. Similar studies on elastic-plastic materials have also been performed by Parks and Zywicz.[11] Rice,[12] in a recent review article, has suggested the concept of 'small-scale contact' which allows the use of the singular models in real situations. Following Hutchinson *et al.*,[13] Rice has also introduced the notion of a complex stress-intensity factor $K = K_1 + iK_2$ in bimaterial fracture studies.

Due to the complexity of the problem, relatively few experimental investigations have been reported. Liechti and Knauss[14] interferometrically studied debonding of a sandwiched elastomer in a uniformly loaded strip. They have observed extensive three-dimensional deformation in such specimens. Liechti *et al.*[15] have reported interferometric measurements and comparisons with complementary finite-element predictions of crack-opening displacement of a bimaterial crack tip. They also report crack-resistance behavior of a glass–epoxy system undergoing different combinations of far-field opening and tangential displacements. Local crack-tip field measurements in a bimaterial model made from two photoelastic materials are reported by Chiang *et al.*[16] Crack-tip opening displacement and energy release rate for a ferrite-austenite interface are measured by Tschegg *et al.*[17] Gao and Evans[18] and Charalambides *et al.*[19] have used hybrid methods to infer mode mixity and complex stress-intensity factors by boundary measurements followed by analytical and numerical modeling.

In this report we present an experimental investigation of the local interfacial crack-tip fields. The bimaterial system used in the study (PMMA-Aluminum) has a relatively large stiffness mismatch. The experimental method adopted is the newly developed shearing interferometry - coherent gradient sensing (CGS), that can be used both in a reflection mode (for opaque solids) and in a transmission mode (for isotropic transparent solids).[20,21] This noncontact, real-time and full-field optical technique has shown great promise in the study of quasi-static as well as dynamic crack-tip fields in homogeneous materials.[21,22] In this report, we present an extension of this method to the investigation of interfacial cracks. The deformation

H.V. Tippur is Assistant Professor, Department of Mechanical Engineering, 201 Ross Hall, Auburn University, Auburn, AL 36849. A.J. Rosakis is Associate Professor, Department of Aeronautics and Applied Mechanics, California Institute of Technology, 105-50, Pasadena, CA 91125.

Original manuscript submitted: August 20, 1990. Final manuscript received: May 31, 1991.

fields presented here are obtained using the CGS technique in the transmission mode. Quasi-static crack-tip measurements are interpreted using the plane-stress, elastostatic, bimaterial crack-tip fields to measure the complex stress-intensity factor K. This is done by making sure that measurements are performed in regions near the crack tip where the plane-stress assumption is valid. The question of three dimensionality in bimaterial specimens has recently been addressed by Nakamura,[23] Barsoum[24] and Liechti and Chai.[25]

Despite its practical importance, the topic of dynamic failure of bimaterial interfaces has virtually remained unexplored, both theoretically and experimentally. Due to the complexity of the problem, thus far, only a few theoretical reports on dynamic bimaterial crack-tip behavior can be found in the literature.[26-29] These studies strictly provide crack-line solutions. The complete structure of the near-tip fields is still unavailable. Atkinson[26] has treated the interfacial crack under anti-plane shear and plane-strain conditions. Brock and Achenbach[27] have investigated the dynamic rupture of the bond between two half spaces undergoing anti-plane shear deformations. Stresses ahead of the crack tip along the bond line for a steadily propagating interface crack are given by Gol'dshtein[28] and Willis.[29] Besides the $x_1^{-1/2}$ variation along the bond line, the in-plane stresses, σ_{22} and σ_{12}, have an oscillatory component when $x_1 \to 0$, similar to the behavior seen in the quasi-static, plane solution.

On the other hand, there have been no direct experimental measurements of deformation fields near dynamically propagating cracks in bimaterial specimens. Unlike static conditions, in stress-wave-loaded bimaterial specimens, hybrid techniques prove insufficient to model crack growth. In view of these, we have attempted a preliminary optical investigation of deformation fields near dynamically growing cracks along PMMA-aluminum interfaces. Due to the lack of a complete asymptotic description of dynamic deformations near an interface crack, only *estimates* of energy release rate and mode mixity are obtained.

Coherent Gradient Sensing

Experimental Setup

In Fig. 1 the schematic of the experimental setup used for transmission CGS is shown. A transparent, optically isotropic specimen is illuminated by a collimated bundle of coherent laser light. The transmitted object wave is then incident on a pair of high-density Ronchi gratings, G_1 and G_2, separated by a distance Δ. The light field emerging from G_2 is collected by the filtering lens L_1 and its frequency content is displayed on its back focal plane. By locating a filtering aperture around either the ± 1 diffraction orders, information regarding the stress gradients is obtained on the image plane. The camera, consisting of the lens L_1 and image plane, is kept focussed on the object plane. For simplicity, let the magnification factor be unity.

In the following sections, a first-order diffraction analysis is presented to demonstrate that the information displayed on the image plane indeed corresponds to gradients of in-plane stress quantities.

Principle

Figure 2 explains the working principle of the method of CGS. For the sake of simplicity, and without losing generality, the line gratings are assumed to have a sinusoidal transmittance. Let the gratings G_1 and G_2 have their rulings parallel to, say, the x_1 axis. A plane wave transmitted through an undeformed specimen and propagating along the optical axis, is diffracted into three plane wavefronts, E_0, E_1 and E_{-1}, by the first grating, G_1. The magnitude of the angle between the propagation directions of E_0 and $E_{\pm 1}$ is given by the diffraction equation $\theta = \sin^{-1}(\lambda/p)$, where λ is the wavelength of light and p is the grating pitch. Upon incidence on the second grating G_2, the wavefronts are further diffracted into $E_{(0,0)}$, $E_{(0,1)}$, $E_{(1,-1)}$, $E_{(1,0)}$, $E_{(1,1)}$, etc. These wavefronts which are propagating in distinctly different directions, are then brought to focus at spatially separated diffraction spots on the back focal plane of the filtering lens. The spacing between these diffraction spots is directly proportional to $\sin\theta$ or inversely proportional to the grating pitch p.

Now, consider a plane wave normally incident on a deformed specimen. The resulting transmitted wavefront will be distorted due to the deformation induced changes in refractive index. This object wavefront that is incident on G_1 now carries information regarding the specimen deformation, and consists of light rays traveling with perturbations to their initial direction parallel to the optical axis. If a large portion of such a bundle of light has rays nearly parallel to the optical axis, each of the diffraction spots on the focal plane of L_1 will be locally surrounded by a halo of dispersed light field due to the deflected rays. The extent of this depends on the nature of the deformations. By using a two-dimensional aperture at the filtering plane, information existing around one of the spots can be further imaged. Here, an important but subtle point should be noted. Since each of the diffraction spots is surrounded by dispersed light due to the deformation, overlapping of the information could occur on the filtering plane when the deflection of the ray is suffficiently large [i.e., $\geq (\lambda/2p)$]. However, it will be shown in the following sections, this limitation can easily be overcome by the use of higher density gratings.

Analysis

Consider a specimen whose midplane occupies the (x_1, x_2) plane in the undeformed state. Let $\mathbf{e}_i$ denote unit vector along x_i-axis, $(i = 1,2,3)$ (see Fig. 3). When the specimen is undeformed, the unit object wave propagation vector $\mathbf{d}_0 = \mathbf{e}_3$. After deformation, the propagation vector is perturbed and can be expressed by

$$\mathbf{d}_0 = \alpha\mathbf{e}_1 + \beta\mathbf{e}_2 + \gamma\mathbf{e}_3 \tag{1}$$

where $\alpha(x_1,x_2)$, $\beta(x_1,x_2)$ and $\gamma(x_1,x_2)$ denote the direction cosines of the perturbed wavefront. This upon incidence on G_1, whose principal direction is parallel to, say, the x_2 axis, is split into three wavefronts propagating along $\mathbf{d}_0$, $\mathbf{d}_{\pm 1}$ and whose amplitudes $E_0(\mathbf{x}')$, $E_{\pm 1}(\mathbf{x}')$ can be represented by

$$\begin{aligned} E_0(\mathbf{x}') &= a_0 \exp\,[ik\mathbf{d}_0 \cdot \mathbf{x}'] \\ E_{\pm 1}(\mathbf{x}') &= a_{\pm 1} \exp\,[ik\mathbf{d}_{\pm 1} \cdot \mathbf{x}'] \end{aligned} \tag{2}$$

where a_0 and $a_{\pm 1}$ are constants and $k = 2\pi/\lambda$ is the wave number. Due to diffraction by the sinusoidal grating G_1, the propagation directions of the diffracted wavefronts can be related to the direction cosines of the incident

propagation vector through (see Ref. 20 for details)

$$\mathbf{d}_{\pm 1} = [\alpha \mathbf{e}_1 + (\beta \cos\theta \pm \gamma \sin\theta)\mathbf{e}_2 + (\gamma \cos\theta \mp \beta \sin\theta)\mathbf{e}_3] \quad (3)$$

using the diffraction condition $\theta = \sin^{-1}(\lambda/p)$. On the plane G_2 ($x_3' = \Delta$) (see Fig. 3), the amplitude distribution of the three diffracted wavefronts are

$$E_0|_{x_3'=\Delta} = a_0 \exp\left[ik\left(\frac{\Delta}{\gamma}\right)\right] \quad (4)$$

$$E_{\pm 1}|_{x_3'=\Delta} = a_{\pm 1} \exp\left[ik \frac{\Delta}{(\gamma \cos\theta \mp \beta \sin\theta)}\right] \quad (5)$$

The wavefronts E_0, $E_{\pm 1}$ will undergo further diffraction upon incidence on G_2 into secondary wavefronts $E_{(0,0)}$, $E_{(0,1)}$, $E_{(1,-1)}$, $E_{(1,0)}$, $E_{(1,1)}$, etc. Of these secondary diffractions, $E_{(0,1)}$ and $E_{(1,0)}$ have their propagation direction along $\mathbf{d}_1$, $E_{(0,-1)}$ and $E_{(-1,0)}$ along $\mathbf{d}_{-1}$ and $E_{(0,0)}$, $E_{(-1,1)}$ and $E_{(1,-1)}$ along $\mathbf{d}_0$ (Fig. 2). If information is spatially filtered by blocking all but ± 1 diffraction order, only the wavefronts $E_{(0,\pm 1)}$ and $E_{(\pm 1,0)}$ contribute to the formation of the image. Noting that the two wavefronts do not acquire any additional relative phase differences after G_2, the amplitude distribution on the image plane is $E_{im} = (E_0 + E_{\pm 1})|_{x_3'=\Delta}$. Hence, the intensity distribution on the image plane under small θ and paraxial approximations ($\gamma \approx 1$) is

$$I_{im} = E_{im}E_{im}^* \approx a_0^2 + a_{\pm 1}^2 + 2a_0 a_{\pm 1} \cos(k\Delta\beta\theta) \quad (6)$$

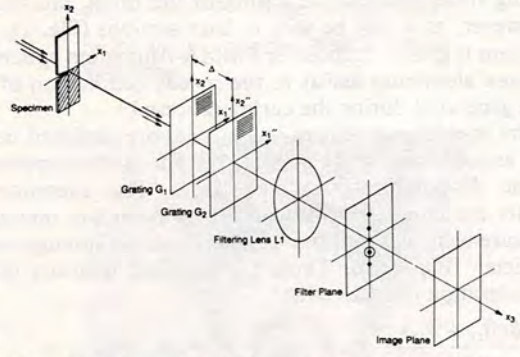

Fig. 1—Schematic of the experimental setup for transmission CGS

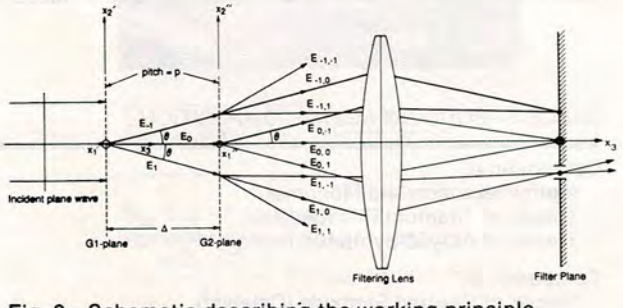

Fig. 2—Schematic describing the working principle of CGS

where E_{im}^* is the complex conjugate of E_{im}. The maxima of the intensity variation I_{im} occurs when

$$k\Delta\beta\theta = 2n\pi \qquad n = 0, \pm 1, \pm 2, \ldots . \quad (7)$$

where n denotes fringe orders. Similarly, when the principal direction of the grating is parallel to the x_1 axis, it can be shown that

$$k\Delta\alpha\theta = 2m\pi \qquad m = 0, \pm 1, \pm 2, \ldots . \quad (8)$$

Equations (7) and (8) are the governing equations for the method of CGS and they relate fringe orders to the direction cosines of the object wavefront. It is clear from the above two equations that the sensitivity of the method could be increased by either increasing the grating separation distance Δ or decreasing the grating pitch p.

Relation Between Direction Cosines and Deformation in Transmission CGS

We now relate the direction cosines of the object wavefront to deformation quantities. Consider a planar wavefront incident normal to an optically isotropic, transparent plate of uniform nominal thickness h and refractive index n_0. Now, if the plate is deformed, the transmitted wavefront acquires an optical path change δS which is given by the elasto-optical equation[30]

$$\delta S = 2h\left(D_1 - \frac{\nu}{E}(n_0 - 1)\right)\int_0^{1/2} \left\{(\sigma_{11} + \sigma_{22})\left[1 + D_2\left(\frac{\sigma_{33}}{\nu(\sigma_{11} + \sigma_{22})}\right)\right]\right\} d(x_3/h) \quad (9)$$

where D_1 and D_2 are elasto-optical constants, σ_{ij} are stress components and E and ν are the Young's modulus and the Poisson's ratio of the material, respectively. The above equation is written in such a way that the second term in the square brackets represents the degree of plane strain. When plane stress is a good approximation, this term can be neglected and eq (9) reduces to

$$\delta S \approx ch(\hat{\sigma}_{11} + \hat{\sigma}_{22}) \quad (10)$$

where $c = D_1 - \frac{\nu}{E}(n_0 - 1)$ and $\hat{\sigma}_{11}$ and $\hat{\sigma}_{22}$ are thickness averages of stress components of the material. Using these, the propagation vector for a perturbed wavefront can be expressed as

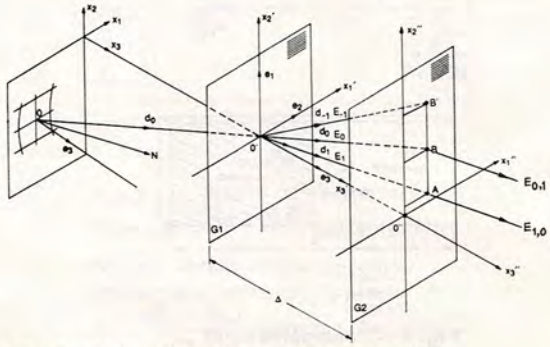

Fig. 3—Diffraction of a generic ray in CGS

$$\mathbf{d}_0 = \frac{\nabla(S)}{|\nabla(S)|} \approx \frac{\partial(\delta S)}{\partial x_1}\mathbf{e}_1 + \frac{\partial(\delta S)}{\partial x_2}\mathbf{e}_2 + \mathbf{e}_3 \quad (11)$$

for $|\nabla(\delta S)|^2 << 1$ and where $S(x_1,x_2,x_3) = x_3 + \delta S(x_1,x_2) = \text{constant}$. Using eq (10) in eq (11), we can obtain the direction cosines of the propagation vector. Thus, using eqs (7) and (8), the fringes can be related to the gradients of $(\hat{\sigma}_{11} + \hat{\sigma}_{22})$ as

$$ch\frac{\partial(\hat{\sigma}_{11} + \hat{\sigma}_{22})}{\partial x_1} \approx \frac{mp}{\Delta} \quad (12)$$

$$ch\frac{\partial(\hat{\sigma}_{11} + \hat{\sigma}_{22})}{\partial x_2} \approx \frac{np}{\Delta} \quad (13)$$

Experiments

Bimaterial Specimen Preparation

Bimaterial specimens used in this study are of the symmetric three-point-bending configuration (Fig. 4). They are made from equal thickness sheets (thickness h = 9 mm) of commercially available polymethyl methacrylate (PMMA) (material-1) and Al 6061-T6 (material-2). The two halves of the specimen are machined to ensure square edges and the bond face of aluminum is sand blasted using 10-20 μm size glass beads. Prior to bonding, the two bond surfaces are thoroughly cleaned using alcohol. Bond between the two materials is created using a commercially available* (see Table 1 for details) methyl methacrylate monomer (MMA) (compound-A) which polymerizes at room temperature when mixed with a catalyst (compound-B). This results in a bond material with stiffness characteristics similar to that of material-1. (In the next section a calibration test is performed to verify this conjecture.) The two part compound is mixed in the ratio of 100 parts by weight of MMA monomer and 13 parts by weight of the catalyst. The aluminum face of the bond is coated with a thin layer of the mixture and held against PMMA with a uniform pressure. The bond is cured at room temperature for 48 hours and the resulting thickness of the bond is approximately 100 μm.

Calibration

It is essential to perform tests to ensure that the stiffness characteristics of the bond material conforms with that of PMMA in order to describe the specimen as a bimaterial system. A calibration test is performed using a three-point-bend specimen in which both halves (material-1 and -2) of the specimen are made of equal thickness (h = 9 mm) PMMA sheets and are bonded together using the above described procedure. The experimental results obtained from this specimen are compared with that of a *homogeneous* PMMA specimen (no bond) in the same three-point-bending configuration.

An edge notch of length 25 mm is cut along the bond line using a band saw of thickness approximately 0.75 mm. A 50-mm diameter He-Ne laser beam (λ = 632 nm) is centered around the crack tip and is transmitted through the specimen. The specimen is subjected to three-point bending (P = 1480 N) and the resulting crack-tip deformation field $ch\frac{\partial(\hat{\sigma}_{11} + \hat{\sigma}_{22})}{\partial x_1}$ is recorded using the transmission CGS technique. Other relevant experimental parameters of this test include grating separation distance Δ = 32 mm and grating pitch p = 0.0254 mm. This results in a sensitivity of measurement = 0.025 deg/fringe. It should be mentioned here that the specimen geometry in these tests corresponds to a crack length (a) to plate width (w) ratio of 0.2 which, as shown in an earlier investigation,[21] has a substantial region of K_I-dominance near the crack tip. The extent of K_I-dominance in this specimen exists in the region $0.5 \le r/h \le 1.25$, -180 deg $\le \phi \le 180$ deg where r and ϕ are the crack-tip polar coordinates. The interference patterns obtained from this experiment are shown in Fig. 5(a) while the ones from the *homogeneous* PMMA specimen[21] (P = 1775 N) is shown in Fig. 5(b). Clearly, the fringe patterns are qualitatively similar to one another and the opaque bond line is distinctly visible in Fig. 5(a) as a narrow dark band ahead of the crack tip. (The thickness of the bond in the photograph is slightly exaggerated due to the specimen alignment and diffraction effects by the layer of bond material.) Also, in a narrow strip along the length of the bond some residual fringes, created by the heat generated during room-temperature curing of the bond, are visible. [However, as it will be seen in later sections (Fig. 7), this problem is greatly reduced in PMMA-Aluminum specimens because aluminum assists in the speedy conduction of the heat generated during the curing process.]

The interference fringes in Fig. 5(a) are analyzed under the assumptions that they are from a homogeneous, elastic K_I-dominant crack-tip field. The experimental results are compared with the value from the boundary measurement and with the results from the homogeneous specimen [Fig. 5(b)]. Thus, for the field quantity under consideration one can write[21]

$$ch\frac{\partial(\hat{\sigma}_{11} + \hat{\sigma}_{22})}{\partial x_1} = ch\frac{K_I}{\sqrt{2\pi}} r^{-3/2}\cos(3\phi/2) + O(r^{-1/2}) = \frac{mp}{\Delta} \quad (14)$$

where m denotes fringe orders and K_I is the mode-I

Commercial name: Weldon-10 A&B, manufactured by IPS Corporation, Gardena, CA

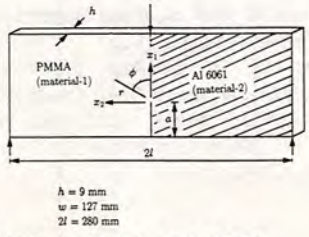

Fig. 4—Three-point-bend bimaterial fracture specimen

TABLE 1—BONDING-AGENT COMPOSITION

Compound-A:
Methyl Methacrylate Monomer
Traces of Titanium Dioxide (Dye)
Traces of Acrylic Synthetic Resin
Compound-B
Traces of Benzoyl Peroxide (Catalyst)
Methyl Ethyl Ketone (Solvent)

stress-intensity factor. Now, let us define a function $Y^{(1)}$ as

$$Y^{(1)}(r,\phi) = \left(\frac{mp}{\Delta}\right)\frac{\sqrt{2\pi}}{ch}\frac{r^{3/2}}{\cos(3\phi/2)} \qquad (15)$$

$Y^{(1)}$ is measurable from the digitized experimental data near the crack tip. It is apparent from the definition of $Y^{(1)}$ and eq (18) that when a K_I-dominant field adequately describes the crack-tip deformations, experimentally measured $Y^{(1)}$ is a constant and is identically equal to the mode-I stress-intensity factor K_I. In Figs. 6(a) and 6(b), $Y^{(1)}$ versus r/h (for different ϕ) are plotted for the interference patterns shown in Figs. 5(a) and 5(b). Note that data in the region -30 deg $< \phi <$ 30 deg are *not* analyzed for Fig. 5(a) in order to avoid the influence of the bond line residual fringes on the crack-tip fringe pattern. It is evident from Fig. 6(a) that for the calibration specimen $Y^{(1)}$ is essentially a constant in region of interest and agrees well with the value of K_I^{2D} obtained from boundary measurements. A similar plot of $Y^{(1)}$ versus r/h for the *homogeneous* specimen is presented in Fig. 6(b). This implies that our earlier conjecture, namely the adopted bonding procedure produces bond material whose stiffness characteristics are similar to those of PMMA, is indeed correct. It should also be noted that the fracture toughness of the bond material is found to be very close to the toughness of PMMA.

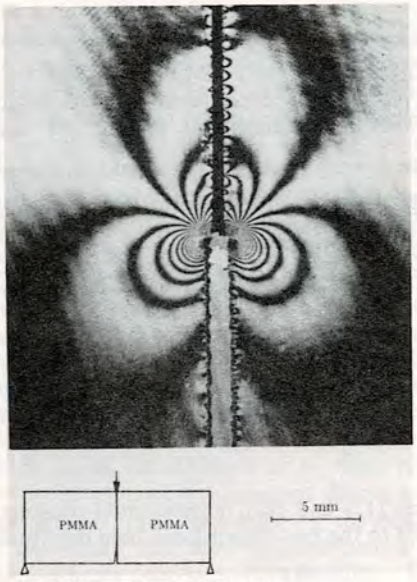

Fig. 5(a)—Fringe patterns representing contours of constant $ch\dfrac{\partial(\hat{\sigma}_{11}+\hat{\sigma}_{22})}{\partial x_1}$ fringes around the notch tip in a bonded PMMA-PMMA specimen

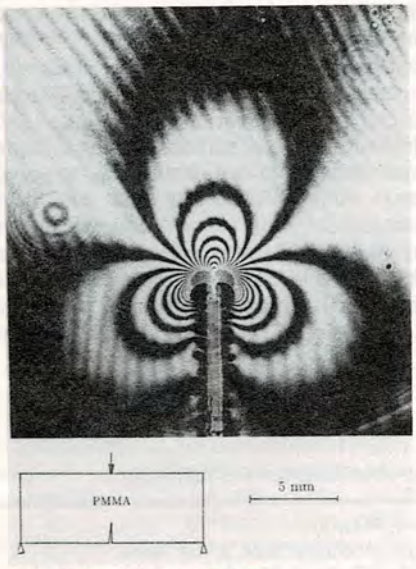

Fig. 5(b)—Fringe patterns representing contours of constant $ch\dfrac{\partial(\hat{\sigma}_{11}+\hat{\sigma}_{22})}{\partial x_1}$ fringes around the notch tip in a homogeneous PMMA specimen

Quasi-static Crack Growth Along PMMA-Aluminum Interfaces

Bimaterial specimens (Fig. 4) are tested in a three-point-bending configuration. A starter edge notch of width 0.75 mm and length 25 mm is cut along the interface. A He-Ne laser beam of diameter 50 mm, centered around the crack tip, is transmitted through the specimen. Naturally, this allows us to measure crack-tip deformations only in the transparent (PMMA) half of the specimen. The specimen is loaded in a displacement-controlled loading device. As the load increases, a crack initiates at the pre-cut notch tip and propagates quasi-statically along the interface. The interference fringes that represent the deformation $ch\dfrac{\partial(\hat{\sigma}_{11}+\hat{\sigma}_{22})}{\partial x_1}$ near the crack tip in PMMA are recorded by a motor-driven 35-mm camera

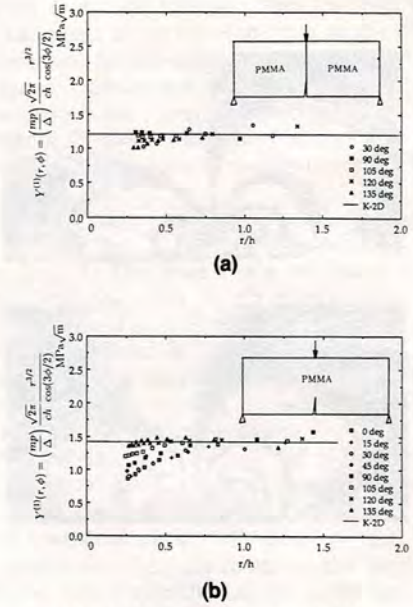

Fig. 6—(a) Plot of Y^1 versus (r/h) from $ch\dfrac{\partial(\hat{\sigma}_{11}+\hat{\sigma}_{22})}{\partial x_1}$ patterns [Fig. 5(a)] for PMMA-PMMA specimen. (b) Plot of Y^1 versus (r/h) from $ch\dfrac{\partial(\hat{\sigma}_{11}+\hat{\sigma}_{22})}{\partial x_1}$ patterns [Fig. 5(b)] for homogeneous PMMA specimen

which at every exposure also triggers a strip-chart recorder to register the corresponding load-cell signal.

In Fig. 7 interference fringes from the bimaterial specimen PAS8 for two different stages of the crack growth, $a/w = 0.21$ and 0.3, are shown. The resolution of measurement is 0.025 deg/fringe. These interference patterns are analyzed using two-dimensional, singular, interfacial crack-tip stress fields given by Rice, Suo and Wang[31] as

$$\sigma_{ij} = \frac{1}{\sqrt{2\pi r}} [Re\{Kr^{i\epsilon}\} \Sigma_{ij}^{I}(\phi,\epsilon) + Im\{Kr^{i\epsilon}\} \Sigma_{ij}^{II}(\phi,\epsilon)] \quad (16)$$

where r, ϕ are the crack-tip polar coordinates and $K = K_1 + iK_2$ is the complex stress-intensity factor. The material mismatch parameter ϵ is given by

$$\epsilon = \frac{1}{2\pi} \ln \frac{\frac{\kappa_1}{\mu_1} + \frac{1}{\mu_2}}{\frac{\kappa_2}{\mu_2} + \frac{1}{\mu_1}}$$

where $\kappa_i = \frac{3 - \nu_i}{1 + \nu_i}$ for plane stress and ν_i and μ_i ($i = 1, 2$) are the Poisson's ratio and shear moduli for material 1 and material 2, respectively. A detailed tabulation of Σ_{ij}^{I} and Σ_{ij}^{II} can be found in Ref. 31. Using eq (16), $\sigma_{11} + \sigma_{22}$ can be written as[32]

$$\sigma_{11} + \sigma_{22} = \frac{2e^{\epsilon(\phi-\pi)}}{\sqrt{2\pi r}\cosh(\pi\epsilon)} [Q_1 \cos(\frac{\phi}{2} + \epsilon \ln\frac{r}{a}) - Q_2 \sin(\frac{\phi}{2} + \epsilon \ln\frac{r}{a})] \quad (17)$$

where $Q_1 = |K| \cos\psi$, $Q_2 = |K| \sin\psi$ and hence $|K| = \sqrt{Q_1^2 + Q_2^2}$. The phase angle ψ using crack length a as the length scale is

$$\psi(a) = \tan^{-1} \frac{Im(Ka^{i\epsilon})}{Re(Ka^{i\epsilon})} \quad (18)$$

When the crack length a changes to a, the phase angle ψ changes to ψ. The two phase angles are related to each other by the following expression.

$$\psi(a) = \psi(a) + \epsilon \ln(a/a) \quad (19)$$

Now, let us also define a new phase angle γ such that

$$\gamma = \tan^{-1}(K_2/K_1) \quad (20)$$

Thus, from eqs (18) and (20), γ could also be interpreted as the phase angle corresponding to a length scale of unity. The field quantity of interest for analyzing the CGS interference patterns in material 1 is $ch \frac{\partial(\sigma_{11} + \sigma_{22})}{\partial x_1}$

By differentiating eq (17) with respect to the x_1 coordinate, we can write

$$ch \frac{\partial(\sigma_{11} + \sigma_{22})}{\partial x_1} = \frac{chr^{-3/2}e^{\epsilon(\phi-\pi)}}{\sqrt{2\pi}\cosh(\pi\epsilon)} [-Q_1 \cos(\frac{3\phi}{2} + \epsilon \ln\frac{r}{a}) - 2\epsilon Q_1 \sin(\frac{3\phi}{2} + \epsilon \ln\frac{r}{a}) + Q_2 \sin(\frac{3\phi}{2} + \epsilon \ln\frac{r}{a}) - 2\epsilon Q_2 \cos(\frac{3\phi}{2} + \epsilon \ln\frac{r}{a})] \quad (21)$$

From eqs (12) and (21), experimental measurements can be related to the two-dimensional field description as

$$\frac{mp}{\Delta} = F(r, \phi; Q_1, Q_2) \quad (22)$$

where function F is given in the right-hand side of eq (21).

The fringe patterns are digitized and fringe order (m) and fringe location (r, ϕ) in the crack-tip region are tabulated. The experimental data can be analyzed using the above mentioned [eq (21)] field only if the measured deformations in the laboratory specimen can be well approximated by the plane-stress description. However, previous experimental and numerical crack-tip studies on homogeneous materials reported in the literature indicate that the crack tip is invariably surrounded by a zone of three-dimensional deformations. Its maximum extent is experimentally shown to extend up to one-half plate thickness.[30] Hence, intuitively one would anticipate a three-dimensional zone to surround the interfacial crack tip also. In the literature, very limited information that sheds light on this aspect, exists. Recently, Nakamura[23] has performed a three-dimensional elastostatic finite-element analysis of a tensile bimaterial strip with a

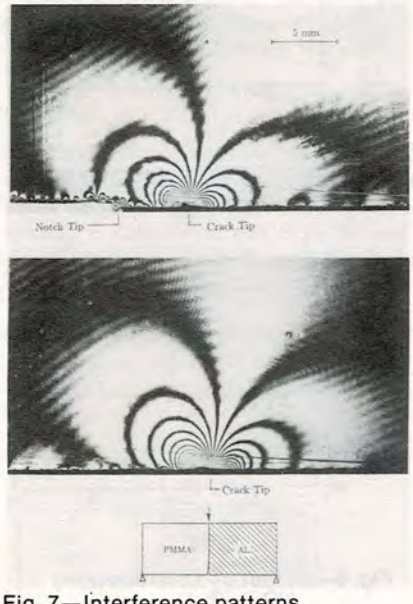

Fig. 7—Interference patterns representing $ch \frac{\partial(\sigma_{11} + \sigma_{22})}{\partial x_1}$ (in PMMA half) near a quasi-statically growing crack along PMMA-aluminum interference; (a) $a/w = 0.21$, (b) $a/w = 0.3$

TABLE 2—MATERIAL PROPERTIES

Material-1: PMMA
Young's Modulus: 3.24×10^3 MPa
Poisson's Ratio: 0.35

Material-2: Al 6061-T6
Young's Modulus: 0.8×10^5 MPa
Poisson's Ratio: 0.3

Plane stress material mismatch: $\epsilon = 0.098$

Griffith crack. Although this study is limited to a narrow class of bimaterial interfaces (*plane strain* $\epsilon = 0$ and *plane stress* $\epsilon \neq 0$), three-dimensional features of the interfacial crack-tip field readily become evident. The study indicates that all along the interface three-dimensional deformations occur and extend up to 1-5 plate thicknesses ahead of the crack tip ($0 \text{ deg} \leq \phi \leq 45$ deg). However, in the region $45 \text{ deg} \leq \phi \leq 150$ deg, three-dimensional deformations seem to decay to a two-dimensional field beyond $r/h \approx 0.5$. This opens up the possibility of using eq (21) for interpreting the experimental data in the region behind the crack tip ($90 \text{ deg} \leq \phi \leq 150$ deg).

Transmission CGS patterns provide information all around the crack tip in the PMMA half (material 1) of the specimen (Fig. 7). However, because three-dimensional deformations are shown to occur in front of the bimaterial crack tip, we will restrict the data analysis, using plane-stress description, to the region $r/h \geq 0.5$, $90 \text{ deg} \leq \phi \leq 150$ deg. A least-square data analysis is performed with $F(r, \phi; Q_1, Q_2)$ as the fitting function to determine Q_1 and Q_2 from the experimental data. Thus, $|K|^{exp}$ ($= \sqrt{Q_1^2 + Q_2^2}$) and γ^{exp} are calculated and are compared with those obtained from plane-stress finite-element calculations performed, on an identical specimen geometry and material mismatch ϵ, by O'Dowd and Shih.[32] Typical comparisons, for two specimens PAS8 and PAS10, are provided in Table 3. From Table 3, it is evident that $|K|^{exp}$ agrees well with $|K|^{FEA}$ obtained from the numerical model for different a/w ratios. Also, note that $|K|^{exp}$ relatively remains constant during the quasi-static crack growth which is similar to the observations of Liechti and Chai[15] who have reported such a behavior under bond-normal displacement loading. However, significant discrepancies seem to persist in the phase-angle measurements. These discrepancies may possibly be attributed to (1) the effect of ϵ ($\neq 0$, both in plane stress and plane strain, in this investigation) on the extent of the three-dimensional zone and/or (2) the influence of higher order terms on the singular crack-tip field in a finite specimen geometry. Additional experimental and numerical investigations are necessary to further explain these observations.

Dynamic Crack Growth Along PMMA-Aluminum Interfaces

Bimaterial specimens used in the dynamic experiments are similar to the ones used in the static experiments. They have a precut edge notch of length 25 mm along the interface. After the initiation event, the crack propagates dynamically along the interface. The bimaterial specimens are impact loaded in a drop-weight tower (Dynatup-8100A) with an impact velocity of 2 m/s. Intense stress waves generated by the impact, loads the notch tip up to crack initiation and the initiated crack propagates dynamically along the interface at speeds up to 700 m/s. The transmission CGS technique is used in conjunction with high-speed photography to record dynamic crack-tip fields in a region approximately 50 mm in diameter around the notch tip. A rotating mirror-type high-speed camera is used in this study. An axially mounted 45-deg mirror, attached to a compressed air-driven turbine shaft, is spun at a high speed. The image is swept on a 35-mm format film (Kodak TMax-400) that is fixed to a stationary drum. Discrete images corresponding to different stages of crack growth are formed by using a pulse laser as the light source. The light source is a Spectra-Physics Argon-Ion pulse laser (model 166). Short pulses of 50-ns duration produce sharp interference patterns during crack growth. The interval between successive light pulses is set at 7 μs (140,000 frames/s) and the total duration over which the laser is 'on' is 750 μs which corresponds to the time period required by the rotating mirror to complete slightly less than one revolution.

The high-speed turbine is brought up to the required speed. The camera shutter is triggered open before the falling weight makes contact with the specimen. When the drop weight contacts the specimen, the laser starts pulsing and the event is recorded on the film track. Unlike in the dynamic crack-growth experiments with homogeneous specimens, experiments conducted with bimaterial specimens pose an additional degree of complexity in conducting the tests. In reality, it is very difficult to impact the specimens exactly along the thin (100 μm) interface. Any slight experimental asymmetry results in an impact either on the aluminum half or the PMMA half of the specimen. Due to the differences in the wave-propagation speeds in the two materials, the dynamic loading histories of the crack tip corresponding to these situations vastly differ from one another. Thus, we had to choose, *a priori*, to impact either the aluminum or the PMMA half of the specimen. In this note, we report one set of results from a dynamic experiment (specimen # PAD10) in which impact occurs on the aluminum half of the specimen at a small distance (5 mm) away from the interface. A typical sequence of crack-tip interference patterns ($\Delta = 44$ mm) of the field quantity $ch \dfrac{\partial(\hat{\sigma}_{11} + \hat{\sigma}_{22})}{\partial x_1}$ in PMMA are shown in Fig. 8. The time $t = 0$ corresponds to crack initiation. From the crack length a versus time t record, the crack velocity $\dot{a}$ is inferred. Plots of a versus t and $\dot{a}$ versus t are presented in Figs. 9(a) and (b). It is evident from these plots that very high velocities are attained by the interfacial crack during the event. The maximum velocity attained by the crack in the region of investigation is approximately 80 percent of the Rayleigh wave speed (c_R) for PMMA. Here it should be noted that, there is a theoretical disagreement regarding the terminal velocity of interfacial cracks. Atkinson[26] predicts a terminal velocity exactly equal to the lower of the Rayleigh wave speeds of the two materials. On the other hand, Willis[29] predicts a terminal velocity that is slightly greater than the lower of the two Rayleigh wave speeds. Close to time $t = 0$, fluctuations in crack velocity (and hence the acceleration changes) are also observable. Intense stress waves emanating from the propagating crack tip are also visible in Fig. 8 as discrete kinks and arcs in otherwise smooth fringes. Note the rotation of the fringe lobes with time, particularly prior to crack initiation. This suggests

TABLE 3—QUASI-STATIC CRACK-GROWTH RESULTS

Specimen No.	Load (P) N	a/w	$\lvert K\rvert^{exp}$ MPa$\sqrt{m}$	γ^{exp} deg	$\lvert K\rvert^{FEA}$ MPa$\sqrt{m}$	γ^{FEA} deg
PAS10/8	1928	0.27	1.97	15.7	1.73	29.8
PAS10/10	1898	0.30	2.02	13.5	1.83	28.4
PAS10/12	1869	0.34	1.97	11.4	2.01	27.8
PAS8/8	2320	0.21	2.14	15.2	1.82	30.8
PAS8/10	2290	0.25	2.00	18.7	1.97	29.8
PAS8/12	2250	0.30	2.17	15.1	2.13	25.5

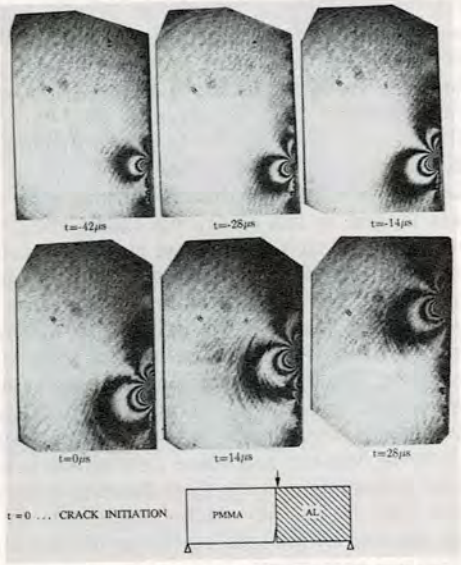

Fig. 8—Interference patterns representing $ch\dfrac{\partial(\hat{\sigma}_{11}+\hat{\sigma}_{22})}{\partial x_1}$ (in PMMA half) near a dynamically growing crack along PMMA-aluminum interface

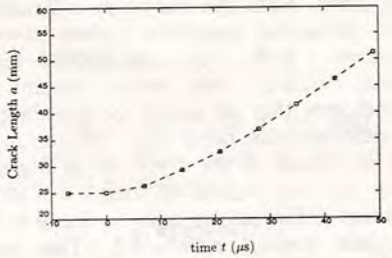

(a)

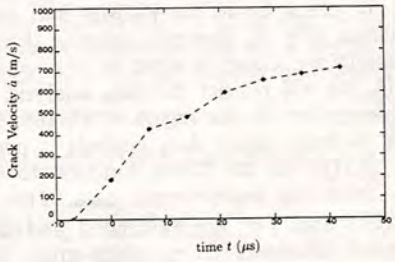

(b)

Fig. 9—(a) Plot of crack length a versus time t. (b) Plot of crack velocity a versus time t for specimen PAD-10

that the crack-tip mode mixity (K_2/K_1) is a constantly changing function during the event.

A systematic interpretation of these fringe patterns is not feasible at this juncture in bimaterial fracture research. Unlike the homogeneous case, there are no dynamic crack-tip field descriptions for bimaterial systems. However, we could *estimate* energy release rate (G^{exp}) and the phase angle (γ^{exp}) from the experimental results. Guided by intuition and the qualitative similarities in the fringe patterns between dynamic and quasi-static crack-growth experiments, we have consciously chosen to make the contestable approximation that these fringes can be interpreted using the available quasi-static field descriptions. This approximation allows us to analyze the dynamic fringe patterns using the procedure described in the previous section. The fringe patterns behind the propagating crack ($r/h \geq 0.5$, $90 \text{ deg} \leq \phi \leq 150 \text{ deg}$) are digitized along different radial directions around the crack tip. Using the least-squares procedure described above, phase angle γ^{exp} and $|K|^{exp}$ from each fringe pattern are measured. Plane-stress energy release rate G is calculated from the definition[6]

$$G = \frac{1}{2}\left(\frac{1}{E_1} + \frac{1}{E_2}\right)\frac{K\bar{K}}{\cosh^2(\pi\epsilon)} \qquad (23)$$

where $\bar{K}$ is the complex conjugate of K and E_1 and E_2 are the Young's moduli for material 1 and 2, respectively. In Figs. 10(a) and (b) plots of γ^{exp} versus t and G^{exp} versus t are shown. As we had observed earlier from the fringe patterns, the crack initiation seems to occur under 'mixed-mode' conditions ($K_2 \approx 1.2K_1$ at $t = 0$). The decrease in γ^{exp} just after crack initiation seems to correspond to a local fluctuation of crack-tip acceleration in Fig. 9(b) soon after crack initiation. With the passage of time, when these transients are attenuated (velocity continuously increasing), a slightly decreasing trend is seen in the phase angle. The variation of G^{exp} with respect to time t [Fig. 10(b)] suggests that, after the initial fluctuations close to $t = 0$, crack propagates with reasonably constant value of G (to within ± 10 percent) although the crack velocity is continuously increasing. The experimental values of quasi-static and dynamic mode mixities [Table 3 and Fig. 10(a)] are significantly different indicating that crack velocity among other transient effects may have a significant influence on dynamic crack growth.

Conclusions

Experimental investigation to study the feasibility of measuring the interfacial fracture parameter, complex stress-intensity factor K, using local crack-tip field quantities is performed. Experiments are conducted on bimaterial systems made of PMMA and Al 6061 sheets. Recently developed optical-technique transmission CGS has been used to measure the deformation fields $ch\dfrac{\partial(\hat{\sigma}_{11}+\hat{\sigma}_{22})}{\partial x_1}$ near quasi-statically and dynamically propagating cracks along bimaterial interfaces. Crack-tip deformations are observed in the PMMA half of the specimen.

Quasi-static crack-tip fringes, in regions where the plane-stress assumptions are valid[23] are analyzed using two-dimensional, interfacial crack-tip fields.[31] Experimentally measured $|K|$ is in good agreement with the numerically calculated values.[32] Also, the crack is quasi-statically propagating at a relatively constant value of $|K|$. However, experimental phase-angle measurements show significant discrepancy when compared with the finite-element counterparts. This could be due to (1) the influence of higher order terms on the crack-tip fields in the finite specimen geometry, and/or (2) the unknown influence of material mismatch parameter (ϵ) on the extent of three-dimensional deformations near the crack tip.

Dynamic crack growth experiments with bimaterial specimens posed an unexpected challenge when impact-loaded three-point-bend specimen geometry was chosen. Due to the difference in the wave propagation speeds in the two materials, impacting either the aluminum half or the PMMA half leads to vastly different dynamic loading histories. One set of results corresponding to the impact loading of the aluminum half, at a small distance 2 mm away from the interface, of the specimen is reported. Very high crack velocities, up to 80 percent of the Rayleigh wave speed of PMMA, are observed. Due to the unavailability of an accepted theoretical model describing the deformation fields near dynamically growing interface cracks, we had to use quasi-static descriptions to *estimate* energy release rate and mode mixity during crack growth. Our limited experimental data suggest a constant G during crack growth, in this bimaterial system although crack velocity is observed to be continuously increasing. The magnitude of mode mixities during dynamic crack growth differs from its quasi-static counterpart suggesting that dynamic effects may significantly influence crack-tip fields.

Acknowledgments

Support of ONR through Contract N00014-90-J-1340 to AJR is gratefully acknowledged. Authors wish to thank Prof. C.F. Shih for his help and several discussions during this investigation. We also like to thank Prof. T. Nakamura for providing us with the information on interface crack-tip three dimensionality. Assistance of Mr. Kenneth Wang during the experiments is gratefully acknowledged.

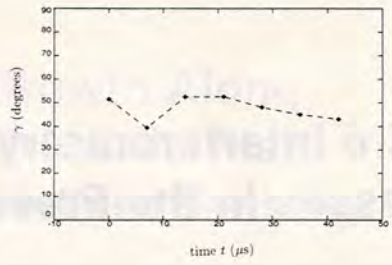

(a)

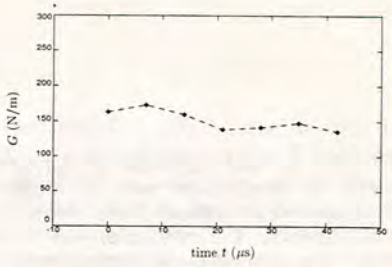

(b)

Fig. 10—(a) Plot of estimated phase angle γ versus time t. (b) Plot of estimated G versus time t for specimen PAD-10

References

1. Williams, M.L., "The Stresses Around a Fault or Crack in Dissimilar Media," Bul. of the Seismological Soc. of Amer., **49** *(2), 199-203 (1959).*

2. Sih, G.C. and Rice, J.R., "Bending of Plates of Dissimilar Materials with Cracks," J. Appl. Mech., **31**, *477-482 (1964).*

3. Rice, J.R. and Sih, G.C., "Plane Problems of Cracks in Dissimilar Media," J. Appl. Mech., **32**, *418-423 (1965).*

4. Erdogan, F., "Stress Distribution in Bonded Dissimilar Materials with Cracks," J. Appl. Mech., **32**, *403-410 (1965).*

5. England, A.H., "A Crack Between Dissimilar Media," J. Appl. Mech., **32**, *400-402 (1965).*

6. Malyshev, B.M. and Salganik, R.L., "The Strength of Adhesive Joints Using the Theory of Crack," Int. J. Fract. Mech., **1**, *114-128 (1965).*

7. Comninou, M., "The Interface Crack," J. Appl. Mech., **44**, *631-636 (1977).*

8. Willis, J.R., "Fracture Mechanics of Interfacial Cracks," J. Mech. Phys. Solids, **19**, *353-368 (1971).*

9. Knowles, J.K. and Sternberg, R.L., "Large Deformation Near a Tip of an Interface-Crack Between Two Neo-Hookean Sheets," J. Elasticity, **13**, *257-293 (1983).*

10. Shih, C.F. and Asaro, R., "Elastic-Plastic Analysis of Cracks on Bimaterial Interfaces; Part-I: Small Scale Yielding," J. Appl. Mech., **55**, *299-316 (1988).*

11. Zywics, E. and Parks, D.M., "Elastic Yield Zone Around an Interfacial Crack Tip," J. Appl. Mech., **56**, *577-584 (1989).*

12. Rice, J.R., "Elastic Fracture Mechanics Concept for Interfacial Cracks," J. Appl. Mech., **55**, *98-103 (1988).*

13. Hutchinson, J.W., Mear, M. and Rice, J.R., "Crack Paralleling an Interface Between Dissimilar Materials," J. Appl. Mech., **54**, *828-832 (1987).*

14. Liechti, K.M. and Knauss, W.G., "Crack Propagation at Material Interfaces: II. Experiments on Mode Interaction," EXPERIMENTAL MECHANICS, **22**, *383-391 (1982).*

15. Liechti, K.M. and Chai, Y-S., "Asymmetric Shielding in Interfacial Fracture Under In-Plane Shear," EMRL Rep. No. 89/4, The Univ. of Texas at Austin (1989).

16. Chiang, F.P., Hua, L. and Yan, X.T., "Photoelastic Analysis of a Crack at a Bimaterial Interface," Advances in Fracture Research, Proc. ICF-7, **4**, *3063-3072 (1989).*

17. Tschegg, H.O., Kirchner, O.K. and Koyak, M., "Cracks at the Ferrite-Austenite Interface," Act. Met. Mat., **38** *(3), 469-478 (1990).*

18. Gao, H.C. and Evans, A.G., "An Experimental Study of the Fracture Resistance of Bimaterial Interfaces," to appear in J. Appl. Mech.

19. Charalambides, P.G., Lund, J., Evans, A.G. and McMeeking, R.M., "A Specimen for Determining the Fracture Resistance of Bimaterial Interfaces," J. Appl. Mech., in press.

20. Tippur, H.V., Krishnaswamy, S. and Rosakis, A.J., "A Coherent Gradient Sensor for Crack Tip Deformation Measurements: Analysis and Experimental Results," Int. J. Fract., **48** *(3), 193-204 (1991).*

21. Tippur, H.V., Krishnaswamy, S. and Rosakis, A.J., "Optical Mapping of Crack Tip Deformations Using the Method of Transmission and Reflection Coherent Gradient Sensing: A Study of Crack Tip K-Dominance," Caltech Rep. SM89-11 (1989). To appear in Int. J. Fract.

22. Krishnaswamy, S., Tippur, H.V. and Rosakis, A.J., "Measurement of Transient Crack Tip Deformation Fields Using the Method of Coherent Gradient Sensing," Caltech Rep. SM90-1 (1990). To appear in J. Mech. Phys. Solids.

23. Nakamura, T., "Three Dimensional Stress Fields of Elastic Interface Cracks," Proc. 11th Nat. Cong. of Appl. Mech., Tucson (1990).

24. Barsoum, R.S., "Three Dimensional Surface Singularity of an Interface Crack," Int. J. Fracture (1990).

25. Liechti, K.M. and Chai, Y.S., "Three Dimensional Effects in Interfacial Crack Growth," Proc. 11th Nat. Cong. of Appl. Mech., Tucson (1990).

26. Atkinson, C., "Dynamic Crack Problems in Dissimilar Media," Mechanics of Fracture - 4: Elastodynamic Crack Problems, ed. G.C. Sih, 230-248 (1977).

27. Brock, L.M. and Achenbach, J.D., "Extension of an Interface Flaw under the Influence of Transient Waves," Int. J. Solids and Struct., **9**, *53-67 (1973).*

28. Gol'dshtein, R.V., "On Surface Waves in Joined Elalstic Materials and Their Relation to Crack Propagation Along the Junction," Appl. Maths and Mech., **31**, *496-502 (1967).*

29. Willis, J.R., "Self-similar Problems in Elastodynamics," Phil. Trans. Roy. Soc., **274**, *435-491 (1973).*

30. Rosakis, A.J. and Ravi-Chandar, K., "On Crack-Tip Stress State: An Experimental Evaluation of Three-Dimensional Effects," Int. J. Solids and Struct., **22** *(2), 121-134 (1986).*

31. Rice, J.R., Suo, Z. and Wang, J.-S., "Mechanics and Thermodynamics of Brittle Interfacial Failure in Bimaterial Systems," Metal-Ceramic Interfaces, Acta-Scripta Met. Proc. Series, **4**, *269-294 (1990).*

32. O'Dowd, N.P. and Shih, C.F., private communications (April 1990).